Journal of Hepatocellular Carcinoma

Dovepress
open access to scientific and medical research

Open Access Full Text Article

ORIGINAL RESEARCH

Immune Effects of Cryoablation in Woodchuck Hepatocellular Carcinoma

Michal Mauda-Havakuk[1,2], Natalie M Hawken[1], Joshua W Owen[1], Andrew S Mikhail[1], Matthew F Starost[3], Baktiar Karim[4], Paul G Wakim[5], Olga L Franco-Mahecha[1], Andrew L Lewis[6], William F Pritchard[1], John W Karanian[1], Bradford J Wood[7]

[1]Center for Interventional Oncology, Radiology and Imaging Sciences, Clinical Center, National Institutes of Health, Bethesda, MD, USA; [2]Interventional Radiology, Tel-Aviv Sourasky Medical Center, Tel-Aviv, Israel; [3]Division of Veterinary Resources, National Institutes of Health, Bethesda, MD, USA; [4]National Cancer Institute, National Institutes of Health, Frederick, MD, USA; [5]Biostatistics and Clinical Epidemiology Service, National Institutes of Health Clinical Center, Bethesda, MD, USA; [6]Alchemed Bioscience Consulting Ltd, Stable Cottage, Monkton Lane, Farnham, Surrey, UK; [7]Center for Interventional Oncology, Radiology and Imaging Sciences, Clinical Center, National Institute of Biomedical Imaging and Bioengineering and National Cancer Institute Center for Cancer Research; National Institutes of Health, Bethesda, MD, USA

Correspondence: Michal Mauda-Havakuk, Email michal.mh@gmail.com

---

Objectives: Local and systemic immune responses evoked by locoregional therapies such as cryoablation are incompletely understood. The aim of this study was to characterize cryoablation-related immune response and the capacity of immune drugs to augment immunity upon cryoablation for the treatment of hepatocellular carcinoma (HCC) using a woodchuck hepatocellular carcinoma model.

Materials and Methods: Twelve woodchucks chronically infected with woodchuck hepatitis virus and with hepatocellular carcinoma underwent imaging with contrast-enhanced CT. Partial cryoablation of tumors in three woodchucks was performed. Fourteen days after cryoablation, liver tissues were harvested and stained with H&E and TUNEL, and immune infiltrates were quantified. Peripheral blood mononuclear cells (PBMC) were collected from ablated and nonablated woodchucks, labeled with carboxyfluorescein succinimidyl ester (CFSE) and cultured with immune-modulating drugs, including a small PD-L1 antagonist molecule (BMS-202) and three TLR7/8 agonists (DSR 6434, GS-9620, gardiquimod). After incubation, cell replication and immune cell populations were analyzed by flow cytometry.

Results: Local immune response in tumors was characterized by an increased number of CD3+ T lymphocytes and natural killer cells in the cryolesion margin compared to other tumor regions. T regulatory cells were found in higher numbers in distant tumors within the liver compared to untreated or control tumors. Cryoablation also augmented the systemic immune response as demonstrated by higher numbers of PBMC responses upon immune drug stimulation in the cryoablation group.

Conclusions: Partial cryoablation augmented immune effects in both treated and remote untreated tumor microenvironments, as well as systemically, in woodchucks with HCC. Characterization of these mechanisms may enhance development of novel drug-device combinations for treatment of HCC.

Plain Language Summary: The tumor microenvironment (TME) incorporates complex immune cell milieus. Tumor ablation can evoke an immune response in the tumor as well as systemically. Most reports, however, demonstrate modest immune activation.

Better elucidation of the tumor microenvironment immune response to ablation was needed in order to promote an effective anti-tumoral response.

In this study, the TME post ablation was analyzed in a multicompartmental fashion to better understand local immune response.

In ablation margins, an abundance of anti-tumoral immune cells could be found. Distant tumors in ablated animals however had an increased number of regulatory immune cells.

More effective response of peripheral blood mononuclear cells to stimulation of immune drugs was demonstrated post ablation.

Strategies to augment more robust anti-tumoral immune responses might include targeting ablation margins with immune-stimulating agents and mitigating regulatory immune effects away from the ablation zone.

Keywords: cryoablation, woodchuck, hepatocellular carcinoma, immune effect, tumor microenvironment, hepatitis B virus

---

Received: 6 July 2023
Accepted: 24 October 2023
Published: 6 November 2023

Introduction

Image-guided minimally invasive cryoablation utilizes focal hypothermia for eradication of local tumors in kidney, lung, liver, breast, prostate, bone, and soft tissue.[1] Cryoablation and other locoregional thermal ablation modalities offer advantages over surgery including lower morbidity and shorter hospital stays as well as repeatability and facile compatibility with other oncologic therapies. Notably, locoregional thermal ablation can evoke systemic anti-tumoral immune responses.[2–4] However, there remains a lack of consensus regarding which locoregional therapy results in the most robust and effective immune response in specific clinical scenarios. Evidence suggests that cryoablation may elicit higher production of proinflammatory cytokines.[5,6] It has also been suggested that cryoablation preserves intracellular tumor antigen integrity[6] in contrast to microwave or radiofrequency ablation which cause more protein denaturation and may reduce the amount of intact tumor antigens.[5]

Most reports focus on systemic or peripheral immunologic effects and not on immunologic changes within cryoablated or untreated lesions. This is due the limited availability of human tumor tissues for analysis. Pretreatment biopsy is not routinely performed in HCC and resection post ablation is usually not warranted.[7] Hence, detailed information regarding immune cell deposition in the cryolesion and in the tumor microenvironment post cryoablation is lacking. Moreover, much of our understanding regarding cryolesion configuration and cell death is derived from in vitro investigations[8] or small animal models such as mice and rats,[5,9] which restrict the use of clinical devices, protocols, and imaging tools. Larger animal models, mostly swine, are used in cryoablation experiments to mimic human tissue geometry and scale as well as to model heat deposition that cannot be readily evaluated in smaller animals. Nonetheless, due to the absence of well-established swine tumor models, only normal tissue, and not tumor tissue has been used in cryoablation experiments in swine.[10,11]

The use of animal tumor models with intact immune systems is paramount to understanding immune effects after cryoablation. Woodchuck hepatitis virus (WHV) closely resembles human hepatitis B virus. Woodchucks (*Marmota monax*) infected with the virus as newborns develop chronic hepatitis. Similar to humans, this infection in woodchucks increases the risk of carcinogenesis, commonly leading to development of hepatocellular carcinoma (HCC). Small HCCs in experimentally induced chronic WHV infection have been observed as early as 9 months of age.[12] The species is widely used in the study of hepatitis and antiviral agents as well as for studies of chemoprevention for HCC.[13] Tumor-bearing woodchucks have been proposed as a model for locoregional therapies such as radiofrequency ablation[14] and transarterial chemoembolization[15–17] but local or systemic adaptive and innate immune responses posttherapy have not been investigated.

The purpose of this study was to investigate multicompartmental local and systemic immune responses induced by partial cryoablation of viral-induced woodchuck HCC tumors performed with clinical devices, treatment algorithms, and imaging modalities. The hypothesis was that cryoablation would lead to alteration of immune cell populations at the ablation site and at distant non-ablated tumors as well as responses of PBMC to immune-stimulatory drugs.

Materials and Methods

Animal Procedures

This study was conducted under an animal use protocol approved by the National Institutes of Health Clinical Center Animal Care and Use Committee in compliance with the US Animal Welfare Regulations, and the National Institutes of Health Guide for the Care and Use of Laboratory Animals (NIH Publications No. 8023, revised 1978). A schematic illustrating the study timeline and procedures is shown in Figure 1A. A total of twelve woodchucks (18–24 months old, 5 males, 7 females) (Northeastern Wildlife, Harrison, Idaho, USA) that had been infected with WHV as newborns (cWHV7P2a inoculum, approximately 10^9 viral particles, administered subcutaneously) were confirmed as tumor-positive prior to acquisition for the study. Woodchucks were individually housed with 12-hour light: dark cycles to avoid potential hibernation effects and provided ad libitum access to food and water. Enrichment was also provided. Woodchucks were sedated and placed under anesthesia as previously described.[15] Imaging with diagnostic ultrasound (US) (Philips iU22, Philips Healthcare Solutions, Bothell, WA) and contrast-enhanced computed tomography (CT) (Philips Brilliance MX8000 IDT 16-section Detector CT, Philips, Andover, MA, USA) was performed on all 12

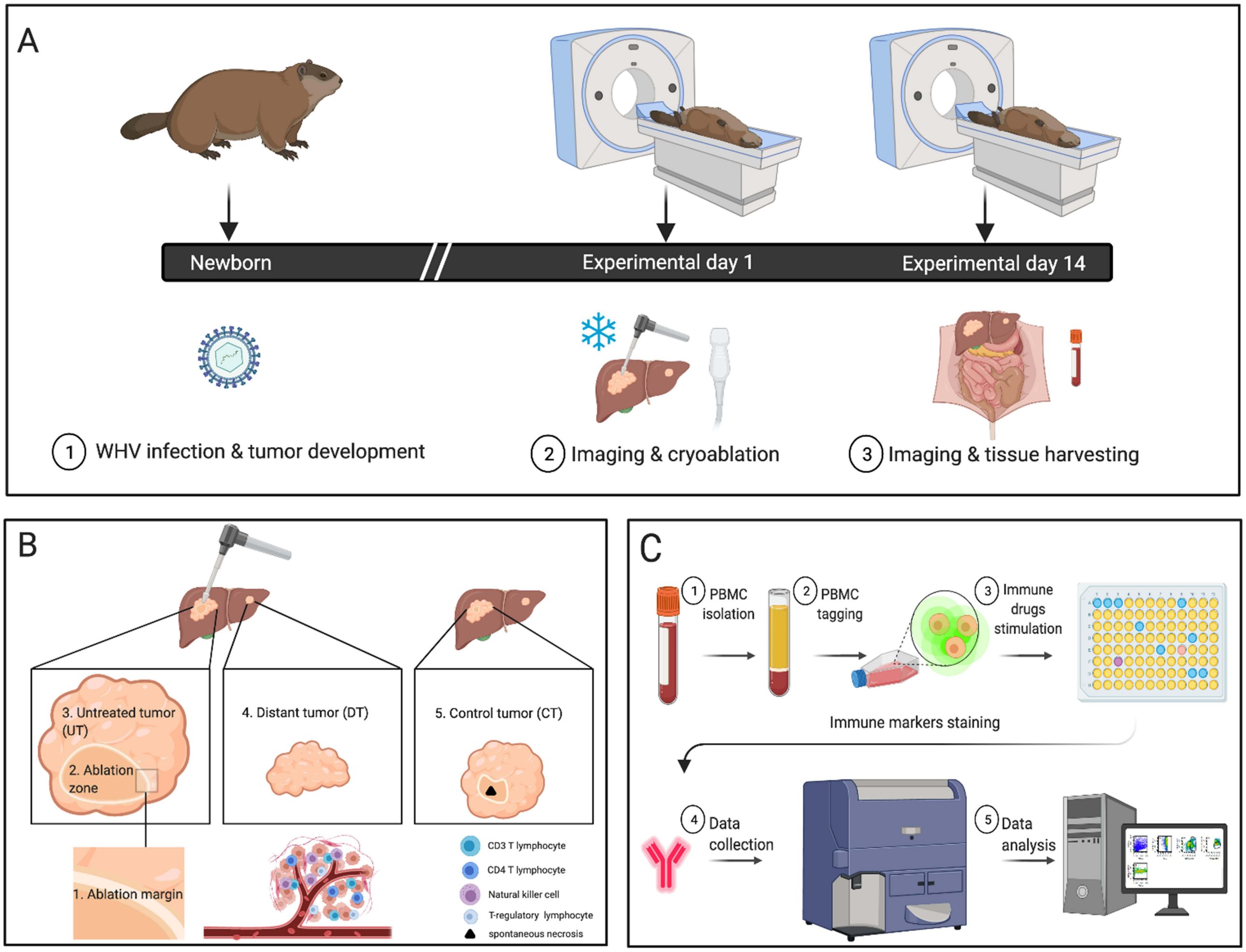

Figure 1 Study design and methods. (**A**) Woodchucks were infected with woodchuck hepatitis virus (WHV) as newborns. At the age of 18–24 months, woodchucks were imaged with computed tomography. Ultrasound guided cryoablation was performed on three animals. Cryoablated woodchucks were imaged and euthanized 14 days after treatment. Whole blood was collected, liver and tumors were sectioned and formalin preserved, and peripheral blood mononuclear cells (PBMC) were purified. (**B**) Tumors were stained for CD3, CD4, NCAM and FOXP3 markers. Immunohistochemical quantification was performed on 5 distinct regions. Three regions were in the ablated tumors: 1. Ablation margin 2. Ablation zone, and 3. Unablated region. The fourth region was located within a separate, untreated tumor (UT) in ablated animals. The fifth region was located in tumors within control, untreated animals (CT) n=9. (**C**) PBMC were purified from whole blood, labeled, cultured with immune-modulating drugs for 4 days and stained with CD3 and CD4 antibodies. FACS analysis was performed and data analyzed for cell replication (n=3 cryoablated animals, n=5 control infected animals, n=2 control uninfected animals).

woodchucks. Vascular access for contrast administration purposes was achieved with insertion of a 21G or 23G angiocatheter into a foreleg vein. Following non-contrast CT of the chest and liver, multiphase imaging of the liver was performed with administration of 3.0 mL iopamidol (Isovue-370, Bracco Diagnostics) followed by 3.0 mL 0.9% saline all at 0.2 mL/sec using power injection (Medrad Stellant CT Injection System, Bayer Healthcare).

Images were analyzed by a board-certified radiologist to confirm presence of LIRADS-4 or −5 HCC to ensure homogeneous stage of disease. The largest liver tumor was identified and documented as the index tumor. Given the limited availability of the animals due to the breeding cycle and time for tumor development, minimal numbers were used in this exploratory study. Nine woodchucks were used as a control group.

Following image acquisition, animals were euthanized by exsanguination while under a surgical plane of anesthesia for blood collection and processing for isolation of PBMC. Tissue was collected for pathology. Of the control animals, six have been reported in a previous work.[18] Partial cryoablation of the index tumor was performed in three woodchucks.[19] The ablation region was planned by a board-certified interventional radiologist with over 25 years of experience to include the solid enhancing region of the index tumor and to avoid complications such as injury to adjacent structures and vessels. Cryoablation was performed using a commercial IcePearl 2.1 CX probe (Boston Scientific, Marlborough, MA) under US guidance. The treatment algorithm was two 10 min freeze cycles, each followed by 8 min thaw in a single location. The probe's heating capability was used to thermally ablate the probe track during withdrawal to prevent hemorrhage. Following cryoablation, non-contrast CT was performed, and animals were recovered. Fourteen days post-cryoablation, woodchucks were sedated, vascular access was achieved, and contrast enhanced CT of the liver was performed as described above. The animals were euthanized as above with blood and tissue collection.

Tissues Collection

Liver tissues for the three cryoablated animals and six control animals were sectioned using tumor-specific, patient-specific 3D-printed sectioning molds designed based on segmentation of in-vivo CT imaging acquired on procedural day 0 as previously described.[20] The specimens from the remaining three control animals were manually cut into 5mm sections. Sectioned tissue blocks were fixed in 10% neutral buffered formalin for a minimum of 24 hours, then processed through a series of increasing concentrations of ethanol, cleared in xylenes, embedded in paraffin blocks and sectioned using a microtome.

Histopathological and Immunohistochemical Analysis

Sequential 5 µm thick sections from the paraffin blocks were mounted onto glass slides (Fisher Scientific, MA, USA). For histologic examination and immune marker immunohistochemical analysis, consecutive tissue sections were obtained from tumors and were independently stained with hematoxylin and eosin (H&E) and terminal deoxynucleotidyl transferase dUTP nick end labeling (TUNEL) (ApopTag Peroxidase In Situ Apoptosis Detection Kit, cat#S7100, Millipore, Burlington, MA), as well as CD3+ (rabbit monoclonal, ab16669), CD4+ (rabbit monoclonal, ab133616), NCAM (mouse monoclonal, ab9018), and FOXP3 (rabbit polyclonal, ab4728) (antibodies provided by Abcam, Cambridge, MA) antibodies. 3, 3-diaminobenzidine (DAB) chromogen stain was used and immunohistochemical slides were then counterstained with hematoxylin. Sections were scanned at 20X using an Aperio AT2 scanner (Leica Biosystems, Buffalo Grove, IL) to create whole slide digital images. Digital image analysis was performed and a total of five regions were classified and annotated by a blinded veterinary pathologist (Figure 1B). An area was annotated within each of the following regions in each ablated tumor: the ablation margin ("Ablation margin"), cryoablated area ("Ablation zone"), and an untreated area of the same tumor ("Untreated tumor (UT)"). A region was annotated within a tumor separate from the index tumor ("Distant tumor (DT)") in each of the woodchucks that underwent cryoablation. A region was annotated within tumors in control woodchucks that were not ablated ("Control tumor (CT)"). Seven animals were used as controls for TUNEL staining and five animals for IHC. Areas of artifact such as folds and tears were excluded from analysis. Quantification of CD3+, CD4+, NCAM, and FOXP3 positive cells were performed with Halo imaging analysis software (Indica Labs, Albuquerque, NM) and the number of positive immune cells per mm^2 was counted. TUNEL stain was calculated as the number of TUNEL positive cells/total cell number (positive + negative) per area using a pixel intensity quantification algorithm with Aperio ImageScope (Leica Biosystems, Cambridge, MA). All tissue taken from woodchucks was proven as hepatocellular carcinoma based on histopathology analysis by a board-certified veterinary pathologist.

PBMC Isolation, Processing and Cryopreservation

Whole blood (45–60 mL) was collected from three cryoablated woodchucks and from five HCC-positive controls in EDTA tubes (Vacutainer EDTA Tubes, BD, cat#367856). Ficoll-Paque (GE Healthcare, cat#17-1441-02) density gradient centrifugation was used to separate PBMC immediately after collection. PBMC were washed in phosphate-buffered saline (PBS) with 1 mM EDTA. Remaining red blood cells were lysed with ACK lysis buffer (Quality Biological, cat#118-156-101) and PBMC were washed in PBS-EDTA twice. PBMC were resuspended in complete AIM-V media (AIM-V, Gibco, cat#12055083) containing 10% heat-inactivated FBS (Hyclone, cat#SH3007003HI), 1% penicillin (10,000 IU/mL), 1% streptomycin (10,000 µg/mL), 1% glutamine (29.3 mg/mL) (Gibco, cat#103787-016) and 1% HEPES buffer (1 M, pH 7.3) (Quality Biological, cat#118-089-721). Cell viability was measured by trypan blue assay. Cells were cryopreserved within FBS-10% dimethylsulfoxide (DMSO) (KD Medical, cat# RGE-3070) in liquid nitrogen.

PBMC from two naïve (not infected with WHV) woodchuck donors (not a part of the 12 experimental animals) were also acquired (BIOSCIENCES, cat#IQB-WPB102).

Immune Stimulators and Controls

Concanavalin-A 2.5 µg/mL (ConA, Sigma, cat#C5275-5MG) was used as a nonspecific stimulant of T cell proliferation. Bovine serum albumin 2.5 µg/mL (BSA; Sigma Chemical Comp., St. Louis, MO) was used as an irrelevant antigen and a negative control. Cells were incubated with four small molecules including a PD-L1 antagonist, BMS-202 (Abcam, Cambridge, MA, cat#ab131311), and TLR7 agonists, DSR 6434 (Tocris Bioscience, Bristol, UK, >98%) and GS-9620 (Advanced ChemBlocks Inc, cat#I-9835), each at concentrations of 0.1, 1, and 10 µg/mL, and TLR7 agonist gardiquimod (Enzo, Farmingdale, NY, ≥98%) at concentrations of 0.3, 3, and 30 µg/mL. All drugs were solubilized in DMSO. PBMC were incubated with the drugs or control substances at 37°C for 4 days.

PBMC Culture

PBMC were removed from liquid nitrogen, thawed in a 37°C water bath, washed twice in cAIMV media, and incubated at 37°C in cAIMV media for 24 hours prior to drug exposure. PBMC ($1*10^6$/mL in PBS) were supplemented with 1.2 µM carboxyfluorescein succinimidyl ester (CFSE) (CellTrace™ CFSE Cell Proliferation Kit, Invitrogen, cat# C34554). The cells were incubated at 37°C for 10 minutes and then washed twice with 10 mL of complete AIM-V. CFSE-labeled PBMC were cultured in triplicate at $1*10^5$ cells/well in 96-well flat bottom tissue culture plates in the presence of three different concentrations of drugs. Controls included CFSE-labeled cells that were not treated with study immune stimulators, as well as untagged cells that were exposed to study immune drugs. Controls were immediately fixed after staining and stored at 4°C until flow cytometry analysis.

Flow Cytometry and Lymphocyte Replication Analysis

PBMC were harvested with ice cold PBS-2mM EDTA and washed with PBS. Triplicates were combined, transferred to a V-bottom tissue plate, and stained with a fixable blue dead stain kit (LIVE/DEAD™ Invitrogen, cat#L34962) for 30 minutes on ice in the dark. Cells were incubated with anti-CD3 (1:20, rat CD3 APC 1F4, BioLegend, cat#201414), and anti-CD4 (1:40, Hu/NHP CD4 BV480 L200, BD, cat#566148) for 45 minutes on ice in the dark using a 5% mixture of normal rat and normal mouse serum in FACS buffer for blocking. Subsequently cells were washed, fixed, and analyzed by flow cytometry (BD, FACSymphony). Cell replication index was analyzed using Modfit software (Verity House Software, Topsham, ME) and was standardized to the negative control in each animal. After the population of interest was gated within the viable cell population, the Cell Tracking Wizard was run to create a model from the data with undivided cells set to peak 0 and the number of generations set to 10. The models and raw data were checked for concordance according to peak number and location. The average number of divisions, percentage of cells in each generation, and the replication index (RI) were recorded. The RI represents the average number of divisions that cells have undergone (Figure 1C). PBMC results from control animals and from two naïve animals were previously reported.[21]

Statistical Analysis

A repeated-measures model was used to assess TUNEL stain as well as immune cell count in IHC taken from the same animal. The dependent variable was defined as stain count, and the independent variable was the region. For TUNEL the regions were as follows: control tumor, spontaneous necrosis in control tumor, untreated tumor (untreated tumor "UT" or distant tumor "DT") and ablation region. Regions for the immune cell count were as follows: ablation margin, ablation zone, untreated tumor "UT", distant tumor "DT", and control tumor "CT" (Figure 1B). Stain counts between different pairs of regions were compared based on *t*-tests applied to differences in least-squares means obtained from the model. Because all reported p-values were unadjusted for multiple comparisons, new p-value thresholds, indicated as a footnote in each table (Tables 1–3), can be considered as reflecting evidence of a difference. A general Bonferroni rule of thumb was used to calculate the new p-value thresholds, ie, 0.05 divided by the number of statistical tests within each block of tests. Repeated-measures models were used to account for the correlation between measurements taken from the same animal in PBMC replication experiments. A standardized replication index (sRI) was created by dividing the RIs by their

Table 1 Differences in TUNEL and Immune Stains Between Regions (Least-Squares Mean, Standard Error, and Confidence Interval for the Difference, and p-value from Testing Whether the Difference Equals 0)

Stain	Region	Region	Estimate	95% CI (Lower, Upper)	P value*
TUNEL	**Necrosis in CT**	**CT**	**0.7**	**0.37, 1**	**0.0007**
	Necrosis in CT	Ablation	−0.07	−0.39, 0.26	0.6571
	Necrosis in CT	**UT**	**0.7**	**0.37, 1**	**0.0008**
	CT	**Ablation**	**−0.75**	**−0.83, −0.67**	**<0.0001**
	CT	UT	0.003	−0.05, 0.05	0.8872
	Ablation	**UT**	**0.75**	**0.69, 0.8**	**<0.0001**
CD3+	Margin	Ablation	160	38.6, 282.8	0.0113
	Margin	**UT**	**241**	**119.65, 363.87**	**0.0003**
	Margin	DT	105	−59.8, 270.87	0.2037
	Margin	**CT**	**181**	**62.3, 299.65**	**0.0038**
	Ablation	UT	81	−41.07, 203.15	0.1867
	Ablation	DT	−55	−220.5, 110.15	0.5028
	Ablation	CT	20	−98.4, 138.9	0.7311
	UT	DT	−136	−301.6, 29	0.1034
	UT	CT	−61	−179.45, 57.9	0.3058
	DT	CT	75	−87.4, 238.3	0.3536
CD4+	Margin	Ablation	−34	−132.3, 64.7	0.4893
	Margin	UT	8	−15.4, 181.6	0.0951
	Margin	DT	53	−80, 187	0.4209
	Margin	CT	102	−27.8, 232.15	0.1154
	Ablation	UT	117	18.45, 215.4	0.0215
	Ablation	DT	87	−46.3, 220.75	0.1926
	Ablation	CT	136	6, 266	0.0415
	UT	DT	−30	−163, 103.8	0.6531
	UT	CT	19	−111, 149	0.7609
	DT	CT	49	−106, 204	0.5243
NK	Margin	Ablation	222	42.9, 402	0.0167
	Margin	**UT**	**388**	**208, 567.5**	**0.0001**
	Margin	**DT**	**473**	**230, 716**	**0.0004**
	Margin	**CT**	**476**	**297, 656**	**<0.0001**
	Ablation	UT	166	−14, 345	0.0697
	Ablation	DT	251	7.5, 494	0.0437

(*Continued*)

Table 1 (Continued).

Stain	Region	Region	Estimate	95% CI (Lower, Upper)	P value*
	Ablation	CT	254	74.5, 434	0.0069
	UT	DT	8	−158, 328	0.4820
	UT	CT	88	−91, 268	0.3241
	DT	CT	3	−240, 246.5	0.9778
FOXP3	Margin	Ablation	6	−4, 16	0.2341
	Margin	UT	−1.4	−11.6, 8.8	0.7855
	Margin	DT	−17	−30, −2.95	0.0186
	Margin	CT	6	−4, 16	0.2391
	Ablation	UT	−7	−17, 2.4	0.1333
	Ablation	**DT**	**−23**	**−36, −9.3**	**0.0015**
	Ablation	CT	−0.06	−10, 9.8	0.9893
	UT	DT	−15	−28.5, −1.8	0.0271
	UT	CT	7.5	−2.5, 17	0.1367
	DT	**CT**	**22.5**	**9.2, 36**	**0.0016**

Notes: *P-values are not adjusted for multiple comparisons. As a general rule of thumb, p-values less than 0.0083 for TUNEL (0.05/6 tests) and 0.0050 (0.05/10 tests) for immune IHC are considered as reflecting evidence of an effect, significant values are bolded. NK= natural killers' cells, FOXP3= T-regulatory cells.

Table 2 Standardized Replication Index (sRI) by Cohort, Stain and Drug (Least-Squares Mean, Confidence Interval, and p-value from Testing Whether the sRI Equals 1)

Cohort	Stain	Drug	Estimate	95% CI (Lower, Upper)	P-value*
Naive	Non-CD3+	BMS	1.005	0.89, 1.12	0.9290
		DSR	**1.383**	**1.25, 1.5**	**<0.0001**
		GS	0.9874	0.9, 1.1	0.8278
		Gard	1.0363	0.9, 1.15	0.5335
	CD3+	**BMS**	**0.8213**	**0.75, 0.88**	**<0.0001**
		DSR	**0.7132**	**0.65, 0.75**	**<0.0001**
		GS	**0.7378**	**0.69, 0.79**	**<0.0001**
		Gard	**0.8761**	**0.82, 0.92**	**<0.0001**
	CD4+	**BMS**	**0.6903**	**0.65, 0.73**	**<0.0001**
		DSR	**0.6445**	**0.6, 0.69**	**<0.0001**
		GS	**0.7349**	**0.7, 0.77**	**<0.0001**
		Gard	**0.6553**	**0.6, 0.7**	**<0.0001**

(*Continued*)

Table 2 (Continued).

Cohort	Stain	Drug	Estimate	95% CI (Lower, Upper)	P-value*
Chronically infected	Non-CD3+	**BMS**	**1.2562**	**1.15, 1.35**	**<0.0001**
		DSR	**1.7181**	**1.6, 1.8**	**<0.0001**
		GS	**1.2882**	**1.18, 1.4**	**<0.0001**
		Gard	**1.2225**	**1.1, 1.33**	**0.0001**
	CD3+	BMS	1.0396	0.99, 1.09	0.1123
		DSR	**0.7945**	**0.75, 0.85**	**<0.0001**
		GS	0.9631	0.9, 1.01	0.1386
		Gard	**1.0914**	**1.05, 1.15**	**0.0004**
	CD4+	BMS	1.1443	0.99, 1.3	0.0594
		DSR	0.9989	0.85, 1.15	0.9884
		GS	1.0336	0.89, 1.18	0.6564
		Gard	0.9397	0.8, 1.1	0.4254
Cryoablated	Non-CD3+	**BMS**	**1.6928**	**1.6, 1.79**	**<0.0001**
		DSR	**1.8019**	**1.7, 1.9**	**<0.0001**
		GS	**1.3847**	**1.3, 1.5**	**<0.0001**
		Gard	**1.2395**	**1.15, 1.3**	**<0.0001**
	CD3+	**BMS**	**0.9007**	**0.85, 0.95**	**0.0003**
		DSR	**0.8489**	**0.8, 0.9**	**<0.0001**
		GS	0.9702	0.9, 1.02	0.2374
		Gard	1.0585	1.008, 1.1	0.0238
	CD4+	**BMS**	**0.7857**	**0.69, 0.88**	**<0.0001**
		DSR	0.9162	0.8, 1.01	0.0881
		GS	0.9341	0.8, 1.03	0.1766
		Gard	**0.7841**	**0.69, 0.88**	**<0.0001**

Notes: *P-values are not adjusted for multiple comparisons. As a general rule of thumb, p-values less than 0.013 (0.05/4 tests) are considered as reflecting evidence of a difference from 1, significant values are bolded.

corresponding negative control (NC) RI. This ratio was analyzed to assess whether the sRIs were different from 1, as follows: three separate models were fitted to the data, one for each of three outcome measures (sRI for non-CD3+, CD3+, and CD4+) as dependent variable, and the following independent variables: drug, drug concentration, animal (ID), animal-by-drug interaction, and drug-by-concentration interaction. All five independent variables were included in the model regardless of their associated p-value. Drug concentrations were defined as low (1×), middle (10×) and high (100×), corresponding to 0.1, 1 and 10 µg/mL for BMS-202, DSR 6434, and GS-9620, and to 0.3, 3 and 30 µg/mL for gardiquimod. The test of whether the sRIs were greater than 1 was based on a *t*-test applied to the sRI's least-squares means and their corresponding standard error, which were obtained from the models. From these same models, sRI least-squares means for individual animals were also estimated for each of the four experimental drugs and each stain. Responses were defined as any test with sRI least-squares mean greater than 1 and unadjusted p-value less than the new,

Table 3 Standardized Replication Index (sRI) for Non-CD3+, CD3+, and CD4+, by Cohort, Animal and Drug (Least-Squares Mean and p-value from Testing Whether the sRI Equals 1)

Cohort	Animal	Drug	Non-CD3+		CD3+		CD4+	
			Estimates	P-value*	Estimates	P-value*	Estimates	P-value*
Naïve	1	BMS	1.05	0.5512	0.85	0.0001	1.02	0.3621
		DSR	**1.89**	**<0.0001**	0.95	0.1204	0.94	0.0388
		GS	1.08	0.3282	0.8	<0.0001	0.98	0.4517
		Gard	1.2	0.0267	0.96	0.3350	0.95	0.1032
	2	BMS	0.96	0.6376	0.8	<0.0001	0.35	<0.0001
		DSR	0.87	0.1423	0.47	<0.0001	0.35	<0.0001
		GS	0.9	0.2029	0.65	<0.0001	0.49	<0.0001
		Gard	0.88	0.1551	0.78	<0.0001	0.35	<0.0001
Chronically infected	1	BMS	**1.65**	**<0.0001**	**1.18**	**0.0015**	1.04	0.8323
		DSR	**2.33**	**<0.0001**	0.83	0.0030	1.13	0.4420
		GS	0.98	0.9128	0.87	0.0232	0.99	0.9842
		Gard	1.18	0.1371	1.14	0.0108	1.18	0.2920
	2	BMS	1.22	0.0706	1.07	0.2027	1.01	0.9132
		DSR	**1.73**	**<0.0001**	0.8	0.0007	0.83	0.3216
		GS	**1.8**	**<0.0001**	0.99	0.8518	0.79	0.2123
		Gard	1.12	0.3049	**1.27**	**<0.0001**	0.8	0.2443
	3	BMS	1.05	0.6399	0.72	<0.0001	1.4	0.0272
		DSR	1.23	0.0554	0.4	<0.0001	**1.6**	**0.0005**
		GS	0.86	0.2753	0.9	0.0709	1.28	0.1000
		Gard	0.85	0.2303	0.65	<0.0001	0.76	0.1557
	4	BMS	1.26	0.0349	**1.23**	**<0.0001**	1.23	0.1729
		DSR	**1.45**	**0.0004**	1.001	0.9773	0.49	0.0034
		GS	1.1	0.3789	0.99	0.8643	1.08	0.6441
		Gard	**1.68**	**<0.0001**	**1.38**	**<0.0001**	0.99	0.9727
	5	BMS	1.09	0.4377	0.99	0.8383	1.05	0.7420
		DSR	**1.8**	**<0.0001**	0.9	0.1711	0.93	0.6763
		GS	**1.68**	**<0.0001**	1.05	0.2458	1.025	0.8850
		Gard	1.27	0.0254	1.008	0.8768	0.96	0.8346

(*Continued*)

Table 3 (Continued).

Cohort	Animal	Drug	Non-CD3+		CD3+		CD4+	
			Estimates	**P-value***	**Estimates**	**P-value***	**Estimates**	**P-value***
Cryoablated	1	BMS	**1.87**	**<0.0001**	0.94	0.2025	0.48	<0.0001
		DSR	**1.64**	**<0.0001**	0.78	<0.0001	0.72	0.0018
		GS	1.2	0.0061	1.1	0.0160	0.92	0.3783
		Gard	**1.4**	**<0.0001**	1.037	0.3947	0.65	0.0002
	2	BMS	**1.7**	**<0.0001**	0.83	0.0003	0.83	0.0501
		DSR	**2.8**	**<0.0001**	0.95	0.2185	1.03	0.7190
		GS	**1.32**	**<0.0001**	0.95	0.4347	0.86	0.0960
		Gard	**1.4**	**<0.0001**	**1.26**	**<0.0001**	0.7	0.0007
	3	BMS	**1.5**	**<0.0001**	0.93	0.1111	1.04	0.6029
		DSR	0.94	0.3779	0.82	0.0001	0.99	0.9846
		GS	**1.63**	**<0.0001**	0.83	0.0005	1.01	0.8319
		Gard	0.89	0.1091	0.88	0.0084	1	0.9692

Notes: *P-values are not adjusted for multiple comparisons. As a general rule of thumb, p-values less than 0.0063 (0.05/8 tests) for Naïve, 0.0025 (0.05/20 tests) for chronically infected, and 0.0042 (0.05/12 tests) for cryoablated are considered as reflecting evidence of a difference from 1, significant values are bolded.

corresponding p-value threshold (see footnote in Table 3). Analyses were done with SAS Version 9.4 software (SAS Institute, Inc., Cary, North Carolina). Statistical analysis was also carried out using GraphPad Prism 8 (GraphPad Software). The significant differences between groups were calculated by one-way ANOVA (Tukey's multiple comparison test). $p < 0.05$ was considered as statistically significant.

Results

Cryolesion Histopathology and Evaluation of Cell Death

Cryoablated tumors were measured on CT images with an average volume of 48.5 cm^3. Histopathological analysis confirmed all ablated tumors to be HCC and further distinguished between three distinct regions in the cryolesions. The central region had coagulative necrosis morphology in two of the lesions (Figure 2A, left and middle panels) while the third cryolesion presented with liquefactive necrosis morphology (Figure 2A, right panel). The central region was surrounded by a layer containing karyorrhectic debris, nuclear fragments, and remnants of neutrophils and macrophages, delineated as a dark purple band surrounding the lesion on the H&E stain (Figure 2A and B). This layer was formed in all cryolesions and appeared continuous and homogeneous when no major bleeding occurred (Figure 2A and B, left panels). By contrast, the layer was disrupted when bleeding occurred within the cryolesion (Figure 2A and B, middle panels). An amorphic pattern of this cell debris layer was observed surrounding the liquefactive necrosis lesion. This layer could be found in the periphery of the cryolesion as well as vacuoles within the central necrosis region (Figure 2A and B, right panels). The third region observable in the cryolesions was the outermost layer which was defined as a rim of coagulative necrosis along with some viable lymphocytes and red blood cells.

Further delineation of the cryolesion was achieved with TUNEL stain which provides DNA fragmentation detection. All regions of the cryolesion, including regions of central necrosis, cell debris and outer coagulative necrosis, were positively stained (Figure 2C). A histologic comparison between regions of planned cell death caused by the partial tumor cryoablation and spontaneous necrosis in untreated control tumors (CT) was performed. As compared to cryolesions in which the necrotic region has a smooth border (Figure 2D), regions of spontaneous necrosis had irregular

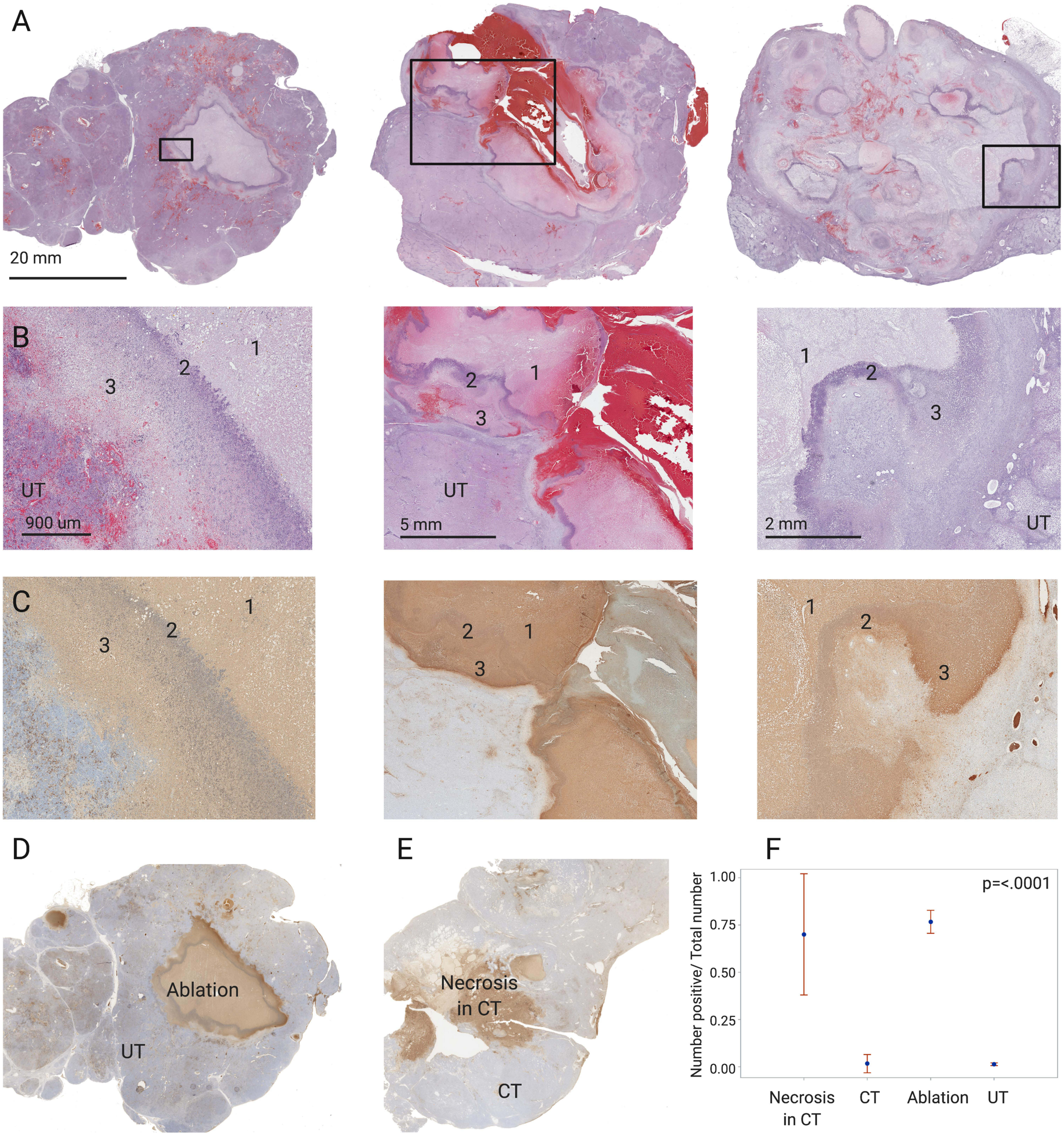

Figure 2 Cryolesion architecture on H&E and TUNEL stains. (**A**) Representative H&E-stained sections of the 3 cryolesions. In the left panel a defined cryolesion with central coagulative necrosis surrounded with a homogenous rim is demonstrated. The middle panel demonstrates a cryolesion with apparent hemorrhage along the needle track and less homogeneous cryolesion rims (reprinted from.[19] with permission). The right panel shows the ablation zone with liquefactive necrosis surrounded by a rim of cell debris that can be found in the central ablation zone as well as in the periphery. Magnified (**B**) H&E-stained and (**C**) TUNEL stained sections of the regions marked in (**A**) delineating the 3 compartments within the cryolesion: central necrosis (1), cell debris rim (2) and coagulative necrosis outer rim (3). Tumor tissue that was not cryoablated is marked with UT (untreated tumor). TUNEL stain annotation was performed on 4 regions. Two regions in the ablated tumor, the ablation zone and untreated tumor (UT), are shown on panel (**D**). Spontaneous necrosis and control tumor (CT) in untreated animals were evaluated as well both regions represented in panel (**E**). (**F**) TUNEL stain quantification, control animals N=7, cryoablated animals N=3, 1–2 sections per animal, p-value for the entire test is shown on the graph. P-values between pairs of regions are summarized in Table 1.

shape and margin as well as areas of cystic degeneration. The peripheral cell debris layer that was seen in the cryolesion was absent (Figure 2E). TUNEL count in cryolesions was comparable to the count in the spontaneous necrosis regions ($p = 0.6571$, Figure 2F and Table 1). Nonetheless, for spontaneous necrosis, the standard error of TUNEL stain was higher with wider range of lower and upper values than in the cryolesions (0.143 vs 0.026 and 0.3–1.02 vs 0.7–0.8 respectively) underlining the predictability and consistency of the killing zone induced by cryoablation. No difference in TUNEL count was observed between control tumors (CT) and untreated tumors (UT) away from the ablation zone ($p = 0.8872$, Table 1) demonstrating that ablation did not induce tissue damage away from the cryolesion.

Local Immune Cell Deposition in Different Tumoral Regions

The distribution and density of immune cells in different tumor regions was evaluated with immunohistochemistry 14 days post partial cryoablation. Two and a half times more CD3+ T-lymphocytes were found in the cryolesions margin compared with the untreated region of the same tumor ($p = 0.0003$, Figure 3, top row). Two times more CD3+ cells were found in the cryolesion margin compared with control tumors ($p = 0.0038$). Two times more CD4+ T-lymphocytes were present in the ablation regions compared to untreated tumors and control tumors ($p = 0.0215$ and $p = 0.0415$ respectively, Figure 3 second row). Natural killer (denoted as NCAM) cells were found in higher numbers in the cryolesion margin compared to all tumor regions, untreated tumor, distant tumors, and control tumors, with 5, 20, and 20-fold increases respectively ($p = 0.0001$, 0.0004, and $p < 0.0001$, Figure 3 third row). Interestingly, a ten-fold increase in T-regulatory cells (denoted as FOXP3) was found in distant tumors compared to control tumors and ablation zone ($p = 0.0016$ and 0.0015, respectively). Summary statistics and p-values for each immune marker are shown in Table 1.

Systemic Immune Responses

Flow cytometric quantification of in vitro woodchuck lymphocyte replication was performed for the innate (non-CD3+), and adaptive (CD3+, and CD4+) cell sub populations (Figure 1C). Unfortunately, woodchuck specific CD8+ fluorescence antibody is not available and thus only the aforementioned cell populations were analyzed. Upon nonspecific T cell stimulation only the cryoablated animals demonstrated increased CD4+ replication (Figure 4). All drugs stimulated non-CD3+ cell replication in vitro in the chronically infected control group and in the cryoablated woodchucks. In the naïve (non-infected) animals only one drug, DSR 6434, induced replication ($p < 0.0001$, Figure 5, upper row). DSR 6434 had the highest magnitude of replication in non-CD3+ cell population across all animal groups. BMS-202 produced a standard replication index (sRI) of 1.26 for non-CD3+ cells in the chronically infected woodchucks and sRI of 1.69 in the cryoablated woodchucks. The only case in which CD3+ cell replication was increased was for gardiquimod in the chronically infected animals' group ($p = 0.0004$, Figure 5, middle row). None of the drugs appeared to increase replication of CD4+ cells for any groups. BMS-202 in the chronically infected group had the strongest effect of increasing replication of CD4+ cells among the four drugs (sRI = 1.14, $p = 0.0594$, Figure 5, bottom row). CD4+ cell replication was decreased in the naïve and cryoablated animals upon incubation with 4 and 2 different immune-modulating drugs, respectively. All p-values for each cell sub-population and drug are shown in Table 2.

There was variability in responses among PBMC from different animals (Figure 6). The greatest number of responses, in terms of non-CD3+ cell replication, was observed in the cryoablated animals' group. Among PBMC samples from 3 animals exposed to the 4 drugs (total of 12 tests) 9 responses were observed. In the chronically infected animals, 8 responses were observed out of 20 tests in contrast to the naïve animals' group in which only 1 out of 8 tests demonstrated a response (Table 3). Four responses out of 20 tests were observed in the CD3+ cell population from chronically infected animals, two for BMS-202 and two for gardiquimod. One response was noted in the cryoablated group upon gardiquimod stimulation. Among all drugs and across groups, only 1 response was observed for CD4+ cells by means of DSR 6434 stimulation in the chronically infected animals. All p-values for each cell sub-population per animal are summarized in Table 3.

Discussion

The immune response in the tumor microenvironment after locoregional therapy is not completely understood. We evaluated the local immune response in a multi-compartmental fashion, as well as the systemic immune response evoked by partial cryoablation. We found that the cryoablation margin is the most immunologically active compartment within the treated tumor and contains an abundance of CD3+ T lymphocytes as well as NK cells. The tumor microenvironment incorporates unique pathological mechanisms with a complex immune cell milieu.[22] Acquisition of human tumor tissue

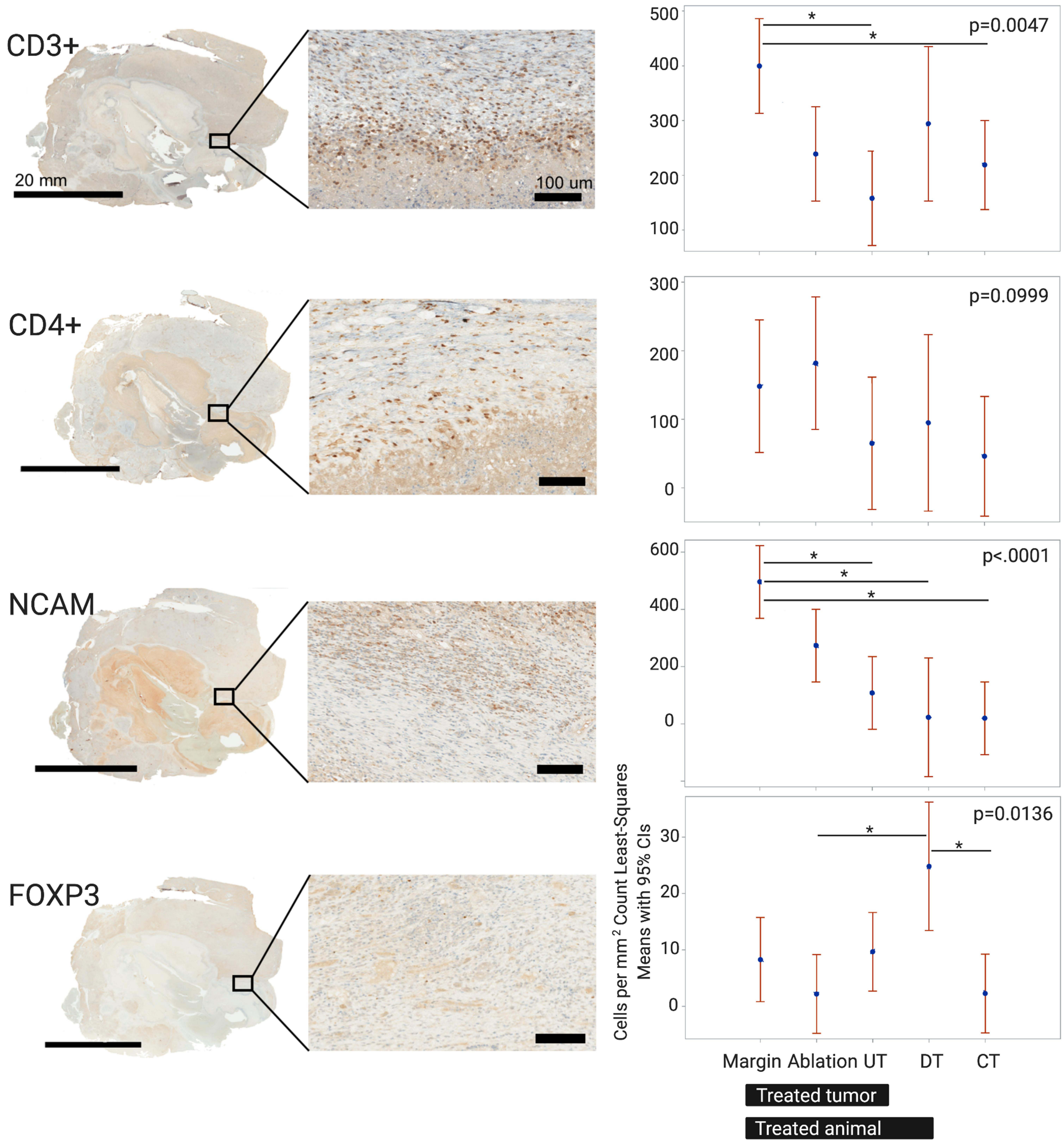

Figure 3 Local immune effects evaluated with immune cell distribution and quantification within the cryolesions. Rows demonstrate immunohistochemical expression and quantification of immune infiltrates, from top to bottom: CD3+, CD4+, NCAM (natural killers' cells) and FOXP3 (T-regulatory cells). Whole mount sections for each stain are shown in the left column with magnification of the cryolesion margin zone in the center column. Quantification for each immune stain by regions as defined in methods and Figure 1B is represented on the right column. Control animals N=5, cryoablated animals N=3, 1–2 sections per animal, p-values for the entire test are shown on the graphs. P-values between pairs of regions are summarized in Table 1.

Abbreviations: UT, untreated portion of treated tumor; DT, distant tumor in treated animal; CT, control tumor in untreated animal.

after locoregional therapy has been mostly limited to tissue biopsies, which may not capture the breadth of the immune response. In this study we present an in-depth immunologic characterization using whole mount tumor specimens following partial cryoablation in a woodchuck HCC tumor model. Pathological analysis revealed distinct regions with distinguishing characteristics within cryoablated tumors.

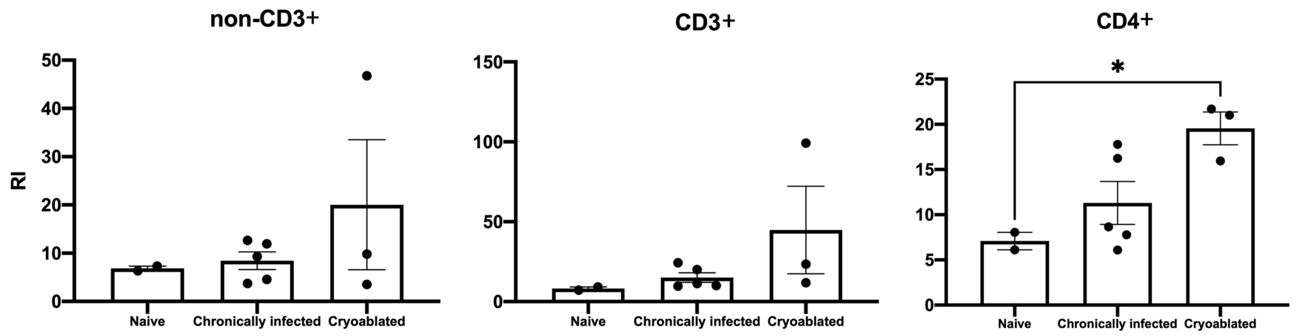

Figure 4 Replication magnitude of PBMC upon nonspecific stimulation in naïve, chronically infected, and cryoablated woodchucks. Evaluation of lymphocyte replication using carboxyfluorescein succinimidyl ester (CFSE) assay in naïve, chronically infected and cryoablated woodchucks for non-CD3+, CD3+, and CD4+ cells. Data represent mean ± SEM. *p<0.05 one-way ANOVA.

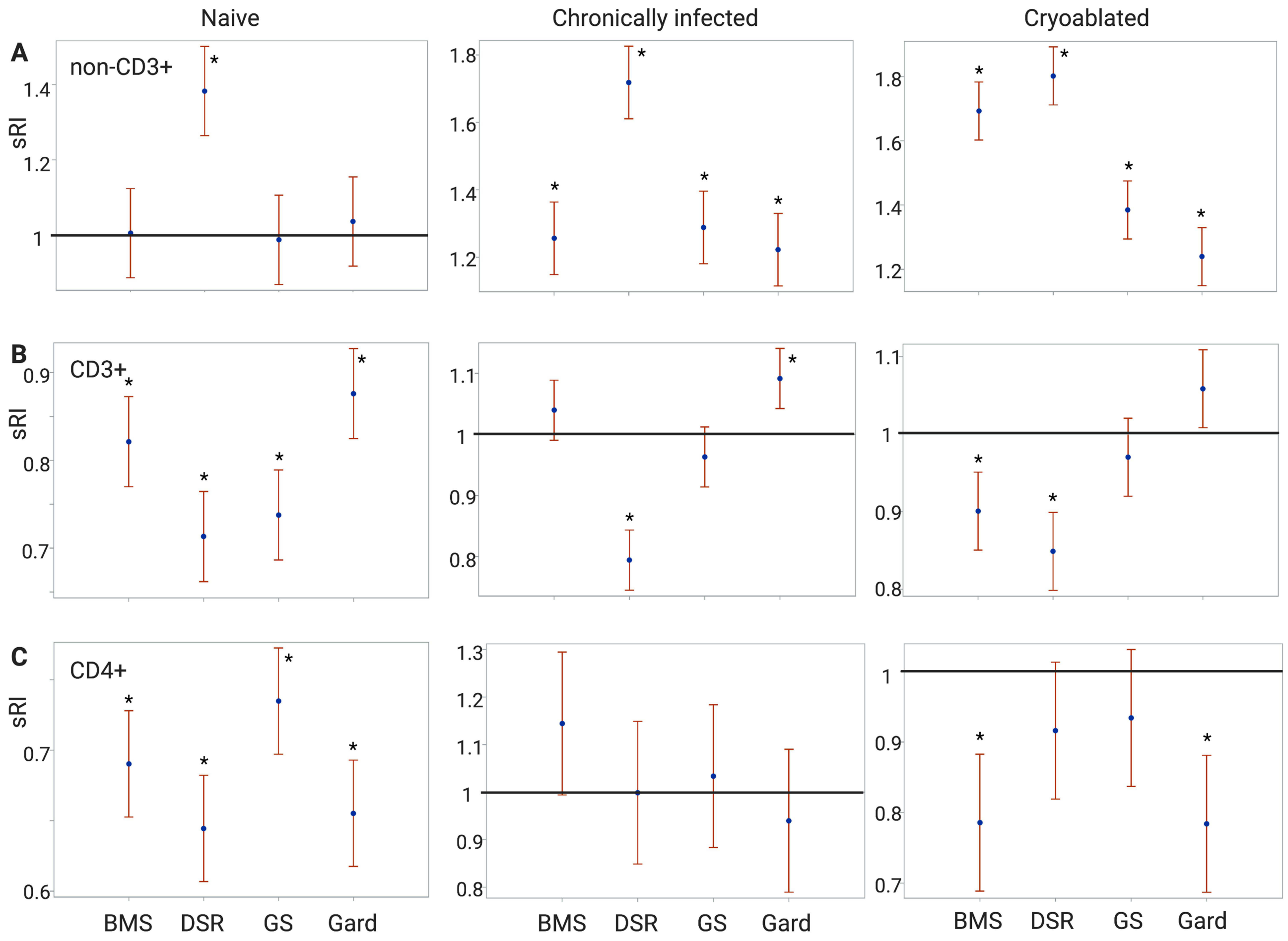

Figure 5 Immune-modulating drug effects on PBMC replication. Evaluation of drug-induced lymphocyte replication using carboxyfluorescein succinimidyl ester (CFSE) assay in naïve, chronically infected and cryoablated woodchucks. The standardized replication index (sRI) is presented for all drugs for non-CD3+ (**A**), CD3+ (**B**), and CD4+ (**C**) sub-populations. The test of whether the sRIs were greater than 1 was based on a *t*-test applied to the sRI's least-squares means and their corresponding standard error, which were obtained from the statistical models. The significant differences between groups were calculated by one-way ANOVA (Tukey's multiple comparison test). p<0.05 was considered as statistically significant and marked by *P-values are summarized in Table 2. BMS= BMS-202; DSR= DSR-6434; GS= GS-9620; Gard= gardiquimod.

Partial cryoablation resulted in a significantly higher number of T-lymphocytes in the cryolesion margin compared to untreated regions of the tumor and distant tumors. Most profoundly this phenomenon was observed with significantly higher numbers of NK cells in the cryolesion margin than any other tumor compartment. Hepatic NK cells can facilitate anti-tumor immunity due to their elevated cytotoxicity levels against tumors,[23] however when exhausted can contribute to HCC tumor immune escape.[24] NK accumulation in the cryolesion post treatment suggests the potential role in enhancing anti-tumoral effects.

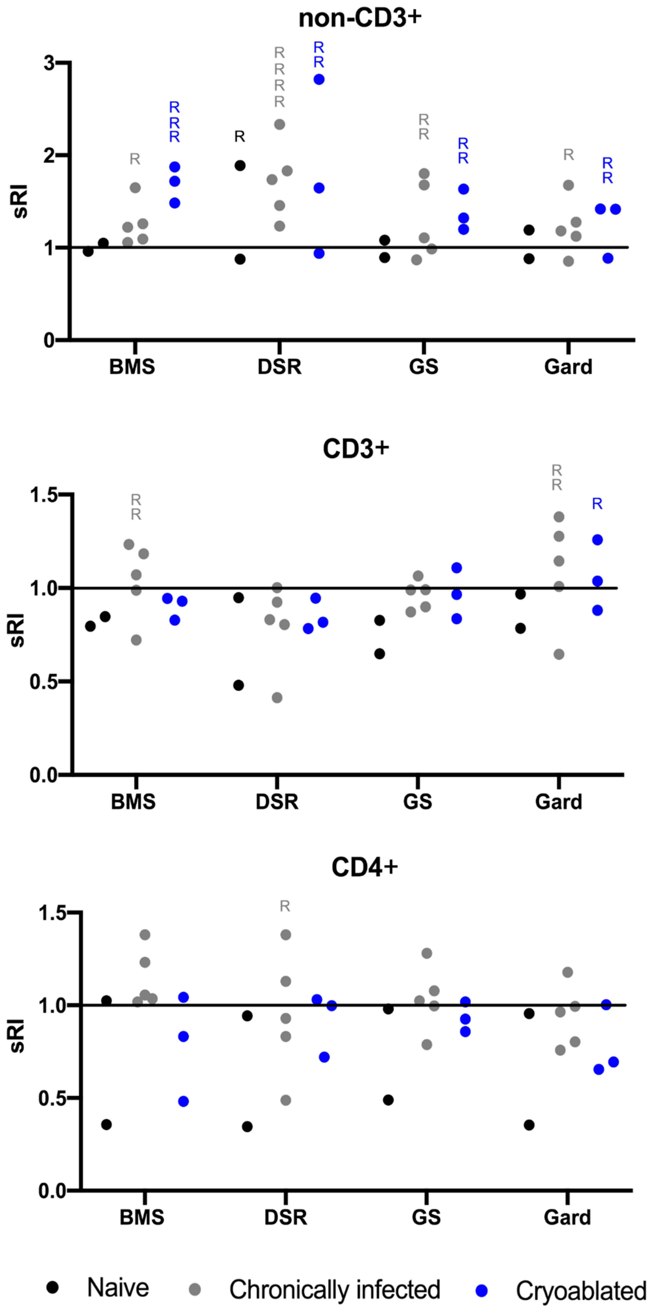

Figure 6 Systemic immune responses by individuals. PBMC from individual woodchucks were evaluated for responses to four experimental immune-modulating drugs. Each combination of woodchuck PBMC sample and a drug comprised a test. Responses were defined as any test with standardized replication index (sRI) least-squares mean greater than 1 and unadjusted p-value < 0.0025 (= 0.05/20 tests). Drug concentrations for each animal were combined and every dot represents the mean sRI. Samples from the same animal cohort are color coded. Any test that fulfilled the response criteria was marked with "R". For example, in the non-CD3+ cell population (top graph) upon DSR 6434 stimulation, 1, 4 and 2 responses were found in the naïve, chronically infected untreated, and the cryoablated woodchucks, respectively. BMS= BMS-202; DSR= DSR-6434; GS= GS-9620; Gard= gardiquimod.

Our data demonstrate that partial tumor cryoablation augmented an immune response that extended beyond local effects, as demonstrated by increased replication capacity of CD4+ T-cells upon nonspecific stimulation. Interestingly, a higher proportion of non-CD3+ cell responses to TLR7 agonists and the PD-L1 antagonist was found in the cryoablation group than any other group. This finding is consistent with an enhancement of anti-tumoral immune responses following combination therapy with cryoablation and immunomodulatory drugs.

Combination of cryoablation and systemic administration of checkpoint inhibitors has demonstrated superior outcomes over each monotherapy in pre-clinical models.[25] The combination has also been shown to be safe and tolerable in small clinical trials[26,27] and is under active investigation in several ongoing clinical trials.[28] In concordance with our results in woodchuck HCC, more CD3+ T cells were present in biopsies of 39 patients with HCC after combination treatment with anti-CTLA4 and transarterial chemoembolization, microwave ablation, radiofrequency ablation (RFA), or cryoablation.[27] A favorable immune environment induced by cryoablation in combination with anti-CTLA4 was further demonstrated by increased activated and proliferating T cells in blood and tumors, respectively, compared to each monotherapy in patients with breast cancer.[26] Immunotherapy with topical TLR7 in combination with tumor cryoablation was reported in melanoma tumors in a murine model. Mice rejected re-challenge tumors in 90% of the cryoablation and TLR7 combination therapy cases, whereas cryoablation alone failed to prevent tumor grafting in 70% of the cases and all mice in the TLR7 alone cohort failed to reject re-challenge tumors.[29] Our data suggest the role of cryoablation as a catalyst for other immunotherapy agents and may lay the groundwork for cryoablation and TLR7 agonists or PD-L1 immune adjuvant combinational therapy.

Pro-oncogenic cryoablation immune effects were also observed in our experiments which may have important implications for selection of combination agents. Our data demonstrated increased number of T-regulatory cells in unablated distant tumors compared to untreated tumors and control tumors. Pro-oncogenic immune effects caused by ablation may be multifactorial. This may include immune suppressive or immune resistance mechanisms, ie, regulatory T cells or pro-growth factors such as IL6, hepatocyte growth factor, or c-Met.[30,31] Nevertheless, these reports might not recapitulate the human clinical scenario. In one study, radiofrequency ablation of normal liver in rats, and not tumoral tissue, resulted in increased growth of subcutaneous breast tumor.[30] In a clinical study, a higher local recurrence rate was observed after RFA in the treatment of colon cancer liver metastasis compared to resection, but the RFA group also had a higher number of liver metastasis per patient and a shorter time from diagnosis to first liver metastasis.[32] Subtotal or incomplete RFA may upregulate immune suppression genes and induce immunosuppressive myeloid cell accumulation in unablated tumor tissue, hinder anti-PD-1 immunotherapy effect, as well as be associated with reduced survival in metastatic colorectal cancer.[33] Pro-oncogenic effects following cryoablation were demonstrated in an orthotopic fibrosarcoma animal model which increased the number of suppressive T cells in the spleen, and had inferior prognosis following cryoablation compared to excisional resection.[34]

Despite aforementioned pro-oncogenic immune effects, a larger body of evidence on the anti-tumoral cryoablation effects has emerged. Cryoablation has been shown to activate antigen presenting cells, glypican-3-specific CTLs, HMGB1, and release immune potentiating antigens into the serum.[35] Cryoablation releases more protein with less denaturation than RFA, which may activate more T-cells when exposed to cell lysates after ablation.[36] Our data promote the understanding of the interplay between anti-tumor and pro-tumor immune effects after cryoablation but further research is needed on the prospect of rational drug selection and optimized approaches for combination therapies.

Given the breadth of opportunities facing interventional oncology, it is clear there is an important role for preclinical animal models. The utility of animal models is paramount to the development of new drugs and drug-device combinations. Animal model investigations enable optimization of drugs and delivery platforms, assessing toxicities of novel therapeutics, and enabling monitoring of longitudinal effects. Few tumor-bearing animal models are of sufficient size to model interventional oncology tools for liver cancer. Woodchucks are the largest to date.[2] They have an intact immune system with HCC spontaneously developing on the background of viral hepatitis and hence may encompass inherent hepatic and tumoral immune evasion mechanisms.[37,38]

While the woodchuck HCC model offers a relevant pre-clinical model, it nonetheless has limited availability which hampers high throughput large scale experiments. One of the limitations of this study is the small sample size of the cryoablated animals. In addition, there remains a lack of validated antibodies such as fluorescent CD8+ antibody and assays for woodchucks which restricts a more robust immune investigation. The degree of inflammation may also not precisely recapitulate human disease with alcoholic, steatotic, or hepatitis induced cirrhosis.

Different subtypes of regulated cell death, ie, apoptosis, necroptosis, ferroptosis and pyroptosis, may evoke different levels of immunogenicity. It has long been debated as to the relative immune merits of necrosis versus apoptosis, which are both temporally and spatially different within and among ablation methodologies.[39] TUNEL labels cells dying by all forms of regulated necrosis[40] and so cannot differentiate between different subtypes of regulated cell death when not used in conjunction with other markers which are currently not validated for woodchucks. Nonetheless, our data show that DNA fragmentation and tumoral cell death co-exist with viable lymphocytes, predominantly in the cryolesion margin.

Conclusions

Local and systemic anti-tumoral and pro-oncogenic immune effects evoked by partial cryoablation in a woodchuck HCC model are demonstrated by increased NK, CD3+ cells, and T-regulatory cells in woodchucks with HCC. In vitro stimulation of PBMC from cryoablated woodchucks with PD-L1 antagonist and TLR7 agonists successfully enhanced systemic innate immune cell replication after tumor cryoablation. These findings may light the way to drug-device combinations that will offer novel avenues and opportunities for informing HCC therapeutic investigation and discovery.

Disclosure

Dr Andrew S Mikhail reports grants from BTG (Now Boston Scientific), during the conduct of the study. Dr William F Pritchard reports the NIH and Boston Scientific Corporation (previously Biocompatibles UK Ltd) have a Cooperative Research and Development Agreement providing support for this research, non-financial support from Northeastern Wildlife, during the conduct of the study. Dr Bradford J Wood reports non-financial support from Philips, non-financial support from Boston Scientific / BTG Biocompatibles, during the conduct of the study; non-financial support, Cooperative Research and Development Agreement [CRADA] from Siemens, grants, non-financial support from NVIDIA, grants, Cooperative Research and Development Agreement [CRADA] from Celsion/Immunon, personal fees from Philips, non-financial support, negotiating Cooperative Research and Development Agreement [CRADA]. Negotiating licensing agreement from Canon Medical, non-financial support, Equipment MTA from Medtronic, grants, Cooperative Research and Development Agreement [CRADA] from XAct Robotics, non-financial support, Equipment MTA from Angiodynamics, non-financial support, Equipment MTA from Imactis, non-financial support, Equipment MTA from Profound MEdical, grants, non-financial support, Cooperative Research and Development Agreement [CRADA] from ProMaxo, non-financial support, Equipment MTA from QT Imaging, non-financial support, Supplies MTA from Theromics, non-financial support, Equipment MTA from MediView, non-financial support, Equipment MTA from Johnson and Johnson, non-financial support, Equipment MTA from Clinical Laserthermia Systems, non-financial support, Supplies MTA from Varian, non-financial support, Equipment MTA from Civco Medical, non-financial support, Equipment MTA from Combat Medical, non-financial support, Equipment MTA from Galvanize, outside the submitted work; In addition, Dr Bradford J Wood has a patent portfolio available upon request with royalties paid to see above. The authors report no other conflicts of interest in this work.

References

1. Cazzato RL, Garnon J, Ramamurthy N, et al. Percutaneous image-guided cryoablation: current applications and results in the oncologic field. *Med Oncol*. 2016;33:140. doi:10.1007/s12032-016-0848-3
2. Greten TF, Mauda-Havakuk M, Heinrich B, et al. Combined locoregional-immunotherapy for liver cancer. *J Hepatol*. 2019;70:999–1007. doi:10.1016/j.jhep.2019.01.027
3. Erinjeri JP, Fine GC, Adema GJ, et al. Immunotherapy and the interventional oncologist: challenges and opportunities-a society of interventional oncology white paper. *Radiology*. 2019;292:25–34. doi:10.1148/radiol.2019182326
4. Llovet JM, De Baere T, Kulik L, et al. Locoregional therapies in the era of molecular and immune treatments for hepatocellular carcinoma. *Nat Rev Gastroenterol Hepatol*. 2021;18:293–313. doi:10.1038/s41575-020-00395-0
5. Jansen MC, van Hillegersberg R, Schoots IG, et al. Cryoablation induces greater inflammatory and coagulative responses than radiofrequency ablation or laser induced thermotherapy in a rat liver model. *Surgery*. 2010;147:686–695. doi:10.1016/j.surg.2009.10.053
6. Chapman WC, Debelak JP, Wright Pinson C, et al. Hepatic cryoablation, but not radiofrequency ablation, results in lung inflammation. *Ann Surg*. 2000;231:752–761. doi:10.1097/00000658-200005000-00016
7. Kim GM, Won JY, Kim MD, et al. Cryoablation of hepatocellular carcinoma with high-risk for percutaneous ablation: safety and efficacy. *Cardiovasc Intervent Radiol*. 2016;39:1447–1454. doi:10.1007/s00270-016-1384-4
8. Yang WL, Addona T, Nair DG, et al. Apoptosis induced by cryo-injury in human colorectal cancer cells is associated with mitochondrial dysfunction. *Int J Cancer*. 2003;103:360–369. doi:10.1002/ijc.10822
9. Yang X, Guo Y, Guo Z, et al. Cryoablation inhibition of distant untreated tumors (abscopal effect) is immune mediated. *Oncotarget*. 2019;10:4180–4191. doi:10.18632/oncotarget.24105
10. Niu L, Li J, Zeng J, et al. Comparison of percutaneous cryoablation with microwave ablation in a porcine liver model. *Cryobiology*. 2014;68:194–199. doi:10.1016/j.cryobiol.2014.01.005
11. Surtees B, Young S, Hu Y, et al. Validation of a low-cost, carbon dioxide-based cryoablation system for percutaneous tumor ablation. *PLoS One*. 2019;14:e0207107. doi:10.1371/journal.pone.0207107
12. Tennant BC, Toshkov IA, Peek SF, et al. Hepatocellular carcinoma in the woodchuck model of hepatitis B virus infection. *Gastroenterology*. 2004;127:S283–S93.
13. Roggendorf M, Kosinska AD, Liu J, Lu M. The woodchuck, a nonprimate model for immunopathogenesis and therapeutic immunomodulation in chronic hepatitis B virus infection. *Cold Spring Harb Perspect Med*. 2015;2015:5.

14. Burke CT, Cullen JM, State A, et al. Development of an animal model for radiofrequency ablation of primary, virally induced hepatocellular carcinoma in the woodchuck. *J Vasc Interv Radiol*. 2011;22(1613):e1. doi:10.1016/j.jvir.2011.08.020
15. Pritchard WF, Woods DL, Esparza-Trujillo JA, et al. Transarterial chemoembolization in a woodchuck model of hepatocellular carcinoma. *J Vasc Interv Radiol*. 2020;31:812–9.e1. doi:10.1016/j.jvir.2019.08.031
16. Kim AY, Yacoub JH, Field DH, et al. Suitability of the woodchuck HCC as a preclinical model for evaluation of intra-arterial therapies. *Animal Model Exp Med*. 2020;3:98–102. doi:10.1002/ame2.12100
17. Wilkins LR, Stone JR, Mata J, et al. The use of the woodchuck as an animal model for evaluation of transarterial embolization. *J Vasc Interv Radiol*. 2017;28:1467–1471. doi:10.1016/j.jvir.2017.04.005
18. Mauda-Havakuk M, Mikhail AS, Starost MF, et al. Imaging, pathology, and immune correlates in the woodchuck hepatic tumor model. *J Hepatocell Carcinoma*. 2021;8:71–83. doi:10.2147/JHC.S287800
19. Esparza-Trujillo JA, Pritchard WF, Mauda-Havakuk M, et al. Imaging and pathologic evaluation of cryoablation of woodchuck (Marmota monax) hepatocellular carcinoma. *Comp Med*. 2023;73(2):127–133. doi:10.30802/AALAS-CM-22-000092
20. Mikhail AS, Mauda-Havakuk M, Partanen A, et al. Liver-specific 3D sectioning molds for correlating in vivo CT and MRI with tumor histopathology in woodchucks (Marmota monax). *PLoS One*. 2020;2020:15.
21. Mikhail AS, Mauda-Havakuk M, Negussie AH, et al. Evaluation of immune-modulating drugs for use in drug-eluting microsphere transarterial embolization. *Int J Pharm*. 2022;616(121466):121466. doi:10.1016/j.ijpharm.2022.121466
22. Roth GS, Decaens T. Liver immunotolerance and hepatocellular carcinoma: patho-physiological mechanisms and therapeutic perspectives. *Eur J Cancer*. 2017;87:101–112. doi:10.1016/j.ejca.2017.10.010
23. Ishiyama K, Ohdan H, Ohira M, et al. Difference in cytotoxicity against hepatocellular carcinoma between liver and periphery natural killer cells in humans. *Hepatology*. 2006;43:362–372. doi:10.1002/hep.21035
24. Han C, Jiang Y, Wang Z, Wang H. Natural killer cells involved in tumour immune escape of hepatocellular carcinomar. *Int Immunopharmacol*. 2019;73:10–16. doi:10.1016/j.intimp.2019.04.057
25. Waitz R, Solomon SB, Petre EN, et al. Potent induction of tumor immunity by combining tumor cryoablation with Anti-CTLA-4 Therapy. *Cancer Res*. 2011;72:430–439. doi:10.1158/0008-5472.CAN-11-1782
26. McArthur HL, Diab A, Page DB, et al. A pilot study of preoperative single-dose ipilimumab and/or cryoablation in women with early-stage breast cancer with comprehensive immune profiling. *Clin Cancer Res*. 2016;22:5729–5737. doi:10.1158/1078-0432.CCR-16-0190
27. Agdashian D, ElGindi M, Xie C, et al. The effect of anti-CTLA4 treatment on peripheral and intra-tumoral T cells in patients with hepatocellular carcinoma. *Cancer Immunol Immunother*. 2019;68:599–608. doi:10.1007/s00262-019-02299-8
28. Yakkala C, Chiang CL, Kandalaft L, et al. Cryoablation and Immunotherapy: an enthralling synergy to confront the tumors. *Front Immunol*. 2019;10:2283. doi:10.3389/fimmu.2019.02283
29. Redondo P, Del Olmo J, Lopez-Diaz de Cerio A, et al. Imiquimod enhances the systemic immunity attained by local cryosurgery destruction of melanoma lesions. *J Invest Dermatol*. 2007;127:1673–1680. doi:10.1038/sj.jid.5700777
30. Ahmed M, Kumar G, Moussa M, et al. Hepatic radiofrequency ablation-induced stimulation of distant tumor growth is suppressed by c-met inhibition. *Radiology*. 2016;279:103–117. doi:10.1148/radiol.2015150080
31. Ahmed M, Kumar G, Gourevitch S, et al. Radiofrequency ablation (RFA)-induced systemic tumor growth can be reduced by suppression of resultant heat shock proteins. *Int J Hyperthermia*. 2018;34:934–942. doi:10.1080/02656736.2018.1462535
32. Tanis E, Nordlinger B, Mauer M, et al. Local recurrence rates after radiofrequency ablation or resection of colorectal liver metastases. Analysis of the European organisation for research and treatment of cancer #40004 and #40983. *Eur J Cancer*. 2014;50:912–919. doi:10.1016/j.ejca.2013.12.008
33. Shi L, Wang J, Ding N, et al. Inflammation induced by incomplete radiofrequency ablation accelerates tumor progression and hinders PD-1 immunotherapy. *Nat Commun*. 2019;10:5421. doi:10.1038/s41467-019-13204-3
34. Wing MG, Rogers K, Jacob G, Rees RC. Characterisation of suppressor cells generated following cryosurgery of an HSV-2-induced fibrosarcoma. *Cancer Immunol Immunother*. 1988;26:169–175. doi:10.1007/BF00205611
35. Helmberger T. The evolution of interventional oncology in the 21st century. *Br J Radiol*. 2020;93:20200112. doi:10.1259/bjr.20200112
36. Shao Q, O'Flanagan S, Lam T, et al. Engineering T cell response to cancer antigens by choice of focal therapeutic conditions. *Int J Hyperthermia*. 2019;36:130–138. doi:10.1080/02656736.2018.1539253
37. Hou J, Zhang H, Sun B, Karin M. The immunobiology of hepatocellular carcinoma in humans and mice: basic concepts and therapeutic implications. *J Hepatol*. 2020;72:167–182. doi:10.1016/j.jhep.2019.08.014
38. Lawal G, Xiao Y, Rahnemai-Azar AA, et al. The immunology of hepatocellular carcinoma. *Vaccines*. 2021;9:1184. doi:10.3390/vaccines9101184
39. Gamrekelashvili J, Kruger C, von Wasielewski R, et al. Necrotic tumor cell death in vivo impairs tumor-specific immune responses. *J Immunol*. 2007;178:1573–1580. doi:10.4049/jimmunol.178.3.1573
40. Janke LJ, Ward JM, Vogel P. Classification, scoring, and quantification of cell death in tissue sections. *Vet Pathol*. 2019;56:33–38. doi:10.1177/0300985818800026